

**Electronic Supplementary Information for:**

## **High-pressure discovery of $\beta$ -NiBi**

Kelly M. Powderly,<sup>‡1</sup> Samantha M. Clarke,<sup>‡1</sup> Maximilian Amsler,<sup>4,5</sup> Chris Wolverton,<sup>4</sup> Christos D. Malliakas,<sup>1</sup> Yue Meng,<sup>2</sup> Steven D. Jacobsen,<sup>3</sup> Danna E. Freedman\*<sup>1</sup>

<sup>1</sup>*Department of Chemistry, Northwestern University, Evanston, Illinois 60208, USA*

<sup>2</sup>*GeoSoilEnviroCARS, Center for Advanced Radiation Sources, The University of Chicago, Chicago, Illinois 60637, USA*

<sup>3</sup>*Department of Earth and Planetary Sciences, Northwestern University, Evanston, Illinois 60208, USA*

<sup>4</sup>*Department of Materials Science and Engineering, Northwestern University, Evanston, Illinois, 60208, USA*

<sup>5</sup>*Present address: Laboratory of Atomic and Solid State Physics, Cornell University, Ithaca, New York 14853, USA*

*Chem. Commun.*

## Table of Contents

<b>Experimental Synthetic Details</b>	<b>S3</b>
<b>Figure S1</b>   Thermodynamic Ni–Bi phase diagram.	<b>S7</b>
<b>Figure S2</b>   SEM and EDS characterization of an $\alpha$ -NiBi crystal.	<b>S8</b>
<b>Figure S3</b>   Schematic of the DAC for <i>in situ</i> reactions.	<b>S9</b>
<b>Figure S4</b>   2D cake image and corresponding integrated PXRD pattern.	<b>S10</b>
<b>Figure S5</b>   Structural comparison of TlI, CrB, and $\beta$ -NiBi.	<b>S11</b>
<b>Figure S6</b>   Structural comparison of NiBi <sub>3</sub> and $\beta$ -NiBi.	<b>S12</b>
<b>Figure S7</b>   Structural comparison of $\alpha$ -NiBi subcell and $\beta$ -NiBi.	<b>S13</b>
<b>Figure S8</b>   Normalized unit cell parameters vs. pressure.	<b>S14</b>
<b>Figure S9</b>   Comparison of high- and low-pressure crystal structures.	<b>S15</b>
<b>Table S1</b>   Refinement details for subcell of $\alpha$ -NiBi.	<b>S16</b>
<b>Table S2</b>   Refinement details for $\beta$ -NiBi at 36.76(4) GPa.	<b>S17</b>
<b>Table S3</b>   Comparison of structural models of $\beta$ -NiBi.	<b>S18</b>
<b>Table S4</b>   Pressure and unit cell parameters of $\beta$ -NiBi during decompression.	<b>S19</b>
<b>References</b>	<b>S20</b>

## Experimental synthetic details

**Synthesis of  $\alpha$ -NiBi single crystals:** We targeted the synthesis of single crystals of  $\alpha$ -NiBi as a starting material for our high-pressure investigations, as they are pure and atomically mixed, thereby eliminating the potential for diffraction from high-pressure bismuth phases. The direct combination of nickel and bismuth in stoichiometric amounts produces polycrystalline samples of  $\alpha$ -NiBi, yet the reaction often yields NiBi<sub>3</sub> as a side product and is not suitable for the synthesis of large single crystals.<sup>1</sup> To successfully isolate large single crystals of  $\alpha$ -NiBi, we developed a Bi self-flux synthesis. Flux-based crystallizations in the solid state are an attractive and useful method for the synthesis of large, intermetallic crystals.<sup>2</sup> The self-flux method, in which one of the reactants is used as the solvent, avoids the presence of other elements that could react to form impurities. Single crystals of  $\alpha$ -NiBi were prepared as follows. Elemental Ni powder (Alfa Aesar, 99.9%, 7.837 mmol, 0.46 g) and Bi powder (Rotometals, 99.9%, 31.287 mmol, 6.5383 g) were ground together under an N<sub>2</sub> atmosphere, placed in an alumina crucible topped with quartz wool, and sealed under vacuum in a quartz ampoule. The mixture was heated to 1000 °C over a period of 15 hours, and reaction was held at that temperature for 24 hours. It was subsequently cooled to 646 °C over a period of 6 hours, then slowly cooled to 475 °C over 12 days. The tube was removed from the furnace at 475 °C then immediately inverted and centrifuged to remove excess molten flux, a mixture of bismuth and nickel (Fig. S1). Once the reaction had cooled to ambient temperature, the ampoule was opened in air and crystals obtained were then soaked in glacial acetic acid for approximately thirty minutes to two hours in order to remove excess bismuth flux present on the surface, polished on 1200 grit silicon carbide paper, and rinsed in isopropyl alcohol. Plate-like single crystals of  $\alpha$ -NiBi up to 2 mm x 2 mm x 0.5 mm in size were obtained from these reactions (Figure S2). To the best of our knowledge these are the largest single crystals of  $\alpha$ -NiBi synthesized thus far.

**Compositional and structural characterization of  $\alpha$ -NiBi single crystals:** Single crystal X-ray diffraction data were obtained at 100 K on a Bruker Kappa APEX2 diffractometer with a Mo K $\alpha$  ( $\lambda = 0.71073$  Å)  $I\mu S$  microfocus source. Data collection, determination of the  $q$ -vector, and unit cell refinement were performed with the program APEX2.<sup>3</sup> Commensurate satellite reflections of the first and second order were utilized for the refinement of the modulated structure using the Jana2006 program.<sup>4</sup> Our solution yielded a commensurately modulated orthorhombic cell with the space group  $Xmma(a00)0ss$ , lattice parameters  $a = 5.3217(3)$  Å,  $b = 8.1281(4)$  Å,  $c = 14.0636(7)$  Å, and a commensurate modulation vector  $q = 1/4a^*$ . The commensurate supercell was solved using a (3 + 1)-dimensional crystallographic approach. Our solution matches very closely with that reported by Ruck.<sup>5</sup>

Scanning electron microscopy (SEM) was performed on a Hitachi S3400N-II scanning electron microscope using a 25 keV accelerating voltage, and energy-dispersive X-ray spectroscopy (EDS) was carried out with an Oxford INCAx-act SSD for semi-quantitative elemental analysis. Crystals were mounted with conductive carbon tape on aluminum stages. Spectra from fifteen points on a polished face of the crystal were averaged to obtain an overall composition. EDS allowed the determination of an atomic ratio of nickel to bismuth of approximately 0.92 to 1, supporting that found from the structural solution and falling within the stoichiometric range established by previous reports.<sup>5,6</sup> Mapping the polished top surface of the crystal with EDS showed both Ni and Bi to be evenly distributed across the sample (Figure S1).

**Diamond anvil cell (DAC) assembly:** A detailed description of the general preparation of the diamond anvil cell (DAC) assembly is summarized in previous publications.<sup>7,8</sup> Briefly, this study employed a tall symmetric diamond anvil cell equipped with two 200  $\mu\text{m}$  culets and a short symmetric diamond anvil cell equipped with two 300  $\mu\text{m}$  culets (Figure S3). The laser micro-machining system at HPCAT enabled us to drill a hole into a pre-indented rhenium gasket.<sup>9</sup> We used thin magnesium oxide (MgO) discs ( $\sim 10\text{--}30$   $\mu\text{m}$ , (111)- oriented) as a thermal insulator, pressure medium, and pressure calibrant during the high-pressure experiments. The error in reported pressure is based on the error in MgO lattice parameters determined from the fit. An MgO disc was placed into the gasket space of the assembled DAC, and a second was placed on the center of the top diamond face. Our sample was a single crystal of  $\alpha\text{-NiBi}$ , which we ground and pressed into a flake by lightly pressing the powder between two 1000  $\mu\text{m}$  culet diamonds. We then transferred the flake on an acupuncture needle into the gasket space, and closed and pressurized the cell.

**Details of *in situ* synchrotron X-ray diffraction:** All experiments were performed at beamline 16-ID-B at the Advanced Photon Source, Argonne National Laboratory, with an incident wavelength of  $\lambda = 0.406626$   $\text{\AA}$ . The synchrotron X-rays were focused to a beam size of  $6.4 \times 5.8$   $\mu\text{m}$  at the center of the laser heating spot. Heating of the sample was performed from both sides of the cell using a microfocused laser (FWHM = 40  $\mu\text{m}$ ), while concurrently acquiring *in situ* X-ray diffraction at the heating spot.<sup>10</sup> Temperatures above  $\sim 550$   $^{\circ}\text{C}$  were measured by fitting the visible portion of the blackbody emission to the Planck radiation function. Diffraction patterns obtained during laser heating were measured with no rotation of the cell and a 2 second exposure time. Diffraction patterns obtained before and after heating were collected while rotating the cell over 10 steps between  $\Omega = -2$  to  $2^{\circ}$ , in order to average over multiple orientations. Diffraction images were obtained with a MAR CCD detector. The pressure drop observed in the heating experiment can be attributed to two sources. First, during the reaction, it is common for the density and volume of the sample to change due to the new structure being formed. Second, small changes of internal pressure during laser heating in a diamond-anvil cell may be attributed to the large amount of laser power (30-100W) and related heat causing plastic flow or creep of the Re gasket.

**Analysis of the X-ray diffraction patterns:** The powder-like character of the new phase allowed for the use of Rietveld methods for structural refinement. The 2D diffraction images were integrated and in some cases background subtracted using the Dioptas software package.<sup>11</sup> Powder X-ray diffraction data were analyzed using the Rietveld method with the software TOPAS.<sup>12</sup> The background was fit using a 6-parameter Chebyshev polynomial. Pseudo-Voigt line broadening was employed for each phase. Preferred orientation was modeled using spherical harmonics. The occupation and thermal parameters of the atoms were held constant due to the difficulty in disentangling these effects from preferred orientation.

Prior to heating, we acquired a powder X-ray diffraction pattern on the pressurized sample of  $\alpha\text{-NiBi}$ . This powder pattern was fit in TOPAS to the NiAs-type subcell structure. Due to the severe peak broadening in the powder pattern, likely induced by the non-hydrostatic pressure applied by the solid pressure-transmitting medium (MgO), we were unable to perform a refinement using a larger supercell

structure. The final refinement parameters for the subcell structure are listed in Table S1. The bond distances discussed in the manuscript were obtained from this structure.

After heating, peaks corresponding to the new high-pressure phase emerged. The indexing procedure was facilitated by the gradual appearance of peaks corresponding to the new phase growing in over the course of several minutes during heating. The most intense peaks were indexed against cubic, hexagonal, trigonal, tetragonal, and orthorhombic unit cells. An orthorhombic unit cell with lattice parameters  $a = 3.873(2) \text{ \AA}$ ,  $b = 9.4079(9) \text{ \AA}$ ,  $c = 3.7587(2) \text{ \AA}$ , and space group  $Cmcm$  was the best match to the data. A search of these lattice parameters in the Inorganic Crystal Structure Database (ICSD)<sup>13</sup> listed a variety of compounds crystallizing in the TII structure type. We used these atomic positions as a starting point for the refinement of  $\beta$ -NiBi. MgO was also present in the powder pattern and refined as a second phase. The final refinement parameters are listed in Table S2.

As noted in the manuscript, there were weak peaks in the PXRD pattern that could not be indexed to the orthorhombic subcell. We hypothesize that these weak peaks correspond to a supercell, suggesting complex superstructure ordering or modulation. To determine if a lower symmetry structure or commensurate supercell structure would improve the refinement significantly, we tried four different structural models (Table S3). Figure S4 shows the predicted  $2\theta$  positions of the  $hkl$  peaks of the orthorhombic supercell (shown in blue), which is generated by tripling the  $b$  lattice parameter. These peak positions match very closely to the weak, unindexed peaks; however Rietveld refinement of this supercell is not significantly better than that of the subcell ( $wR = 4.203$  versus  $4.208$ ), therefore we did not employ this parameter in our final fit. This is likely due a slight misalignment with the weak peak positions, indicating an incommensurate supercell; however, the data quality is not sufficient to solve an incommensurate supercell. We also attempted to lower the symmetry of the cell from orthorhombic to monoclinic. This resulted in only a slight improvement of the residuals ( $wR = 4.064$  versus  $4.208$ ), likely due to the better peak fits obtained by using the monoclinic cell. The minor change indicates the orthorhombic subcell is indeed the best model. We attempted to index the incommensurate supercell using Jana2006.<sup>4</sup> The best indexing was obtained for the pseudo-orthorhombic monoclinic cell with  $C2/m(a0g)00$  symmetry, parameters  $a = 9.3639(6) \text{ \AA}$ ,  $b = 3.3884(2) \text{ \AA}$ ,  $c = 3.7570(2) \text{ \AA}$ , and  $\beta = 89.704(4)^\circ$ , and an incommensurate modulation vector  $q = 0.165841a^* + 0.167984c^*$ . Again, while these peak positions match well with the unindexed peaks, they are not sufficient to refine against due to their extremely weak intensity, and the orthorhombic subcell remains the best model.

After  $\beta$ -NiBi was formed at high pressures, we decreased the pressure incrementally to ambient pressure to determine if the new phase is pressure quenchable, meaning it retains its structure at ambient pressure. Peaks corresponding to  $\beta$ -NiBi were present down to  $11.62(6) \text{ GPa}$ , after which there was a rapid decrease in pressure to  $2.5(1) \text{ GPa}$ , at which peaks belonging to  $\alpha$ -NiBi were present. Rietveld refinements were performed on patterns obtained at each pressure, using the parameters described above (Table S4). Figure S8 depicts the dependence of the lattice parameters of  $\beta$ -NiBi on pressure, normalized to those obtained at  $11.62(6) \text{ GPa}$ , the lowest pressure value.

**Further structural description:** The layered TII structure type ( $B33$ ) is composed of thallium ions coordinated by five iodide ions in a distorted square pyramidal geometry, edge sharing along the  $a$ - and  $c$ -directions. Figure S5 highlights the square pyramids. These 2D sheets stack along the orthorhombic  $b$ -axis. The bonding interaction between the thallium and the iodine at the vertex of the prism ( $3.35(3) \text{ \AA}$ ) is

significantly stronger than the interaction between the thallium and the four iodine atoms lying in the square base of the prism (3.49(1) Å). The Tl–I bonding between the layers (3.86(3) Å) is 15.2% longer than the bonding within the layers (3.35(3) Å, Fig. S5). The interlayer distances between thallium and the two iodine atoms of the adjacent layer (3.86(3) Å) and between thallium atoms (3.83(3) Å) are longer than what would be expected for a true bonding interaction and suggest weak interlayer interactions.

The structure of  $\beta$ -NiBi can be envisioned as a compact version of the TII structure type. Different from TII, the bonding interaction between the nickel and the four bismuth atoms lying in the square base of the prism (2.598(2) Å) is slightly stronger than that between nickel and the bismuth atom at the vertex of the prism (2.632(9) Å). Additionally, the nickel atom is significantly more puckered away from the base of the square prism than what is seen in TII (Figure S5). The interaction between nickel and the two bismuth atoms of the adjacent layer (2.676(7) Å) is only 1.7% longer than the intralayer interaction (2.632(9) Å) suggesting a strong interlayer interaction. In this compact structure, the nickel atom is better described as being coordinated by seven bismuth atoms in a square-face monocapped trigonal prism. Both representations, the distorted square pyramid and the square-face monocapped trigonal prism, are highlighted in Figure S5. Notably, there is a strong Ni–Ni bonding interaction (2.394(8) Å), and the “interlayer” Bi–Bi distance (3.257(3) Å) is within error of the “intralayer” distance (3.252(3) Å), further indication of a compact structure. Since the structure representation of  $\beta$ -NiBi in the main manuscript strongly represents the anti-TII structure type, CrB, this structure is also shown in Figure S5.

**Description of transformation mechanism:** As we observed the first characterized transition from the  $B8_1$  to the  $B33$  structure type, we were interested in elucidating a possible transformation mechanism. An initial step is characterizing the order of a transition; first order transitions occur when change in volume with changing pressure at the transition is discontinuous; otherwise the transition is second or higher order.<sup>14</sup> Within our data, we lack the data density around the transition necessary to determine this order, due to the stepwise, exploratory nature of our experiments. However, we can glean information about our transition by comparing the  $\alpha$ - and  $\beta$ -NiBi structures. In 1951, Buerger proposed classes of transitions based on the degree of change in structure and bonding.<sup>15</sup> In this framework, we can attempt to classify our phase transition as displacive or reconstructive.<sup>16</sup> In the former, atoms move slightly retaining connectivity and bonding, and in the latter, the transformation requires the breaking of bonds. Qualitatively, the general structural motif does not change significantly between  $\alpha$ - and  $\beta$ -NiBi (Figure S7), suggesting a displacive transition. Further, in reconstructive phase transitions, the space groups of the two phases are not subgroups of one another, or are unrelated. The space group of the  $\alpha$ -NiBi subcell is  $P6_3/mmc$  while that of  $\beta$ -NiBi  $Cmcm$ , a subgroup of  $P6_3/mmc$ .<sup>17</sup> This symmetry relationship between the two phases supports that the transition is likely to be displacive. While this analysis was performed using a non-modulated supercell of both phases, future work that solves the potential modulation we observed in  $\beta$ -NiBi may reveal a different symmetry relationship and thus give further insight into the phase transition mechanism.

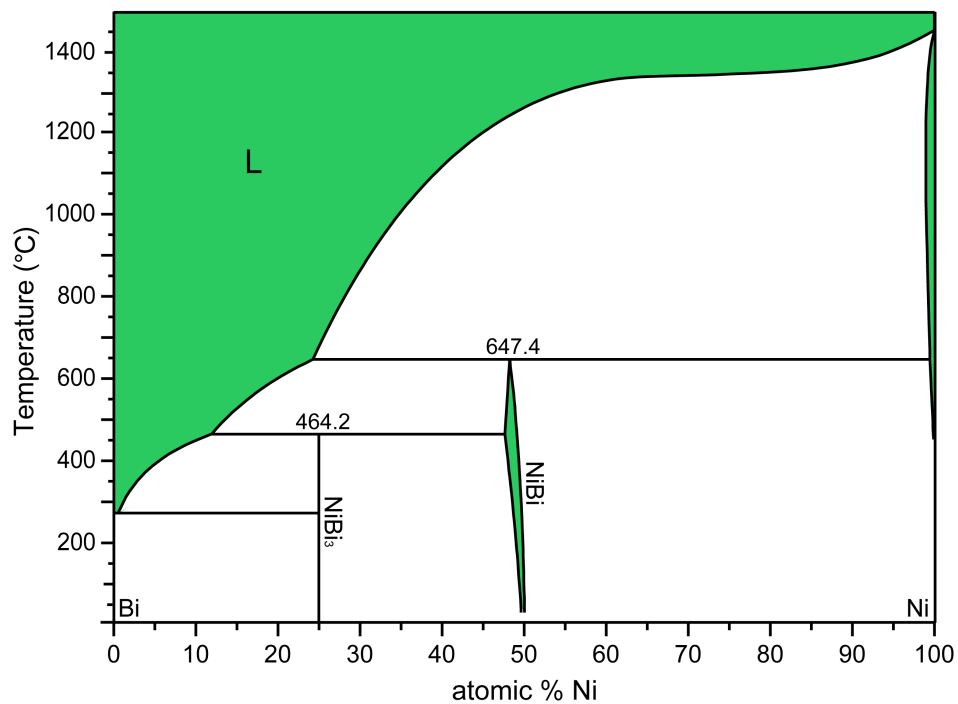


**Figure S1** | Thermodynamic Ni–Bi phase diagram.<sup>18</sup> Two thermodynamically stable intermetallic phases are shown: NiBi<sub>3</sub> and α-NiBi. NiBi<sub>3</sub> is stable at 25% nickel and 75% bismuth up to 464.2 °C. The phase α-NiBi is stable within an appreciable phase width, from approximately 47.5% to 50% nickel, and up to 647.4 °C.

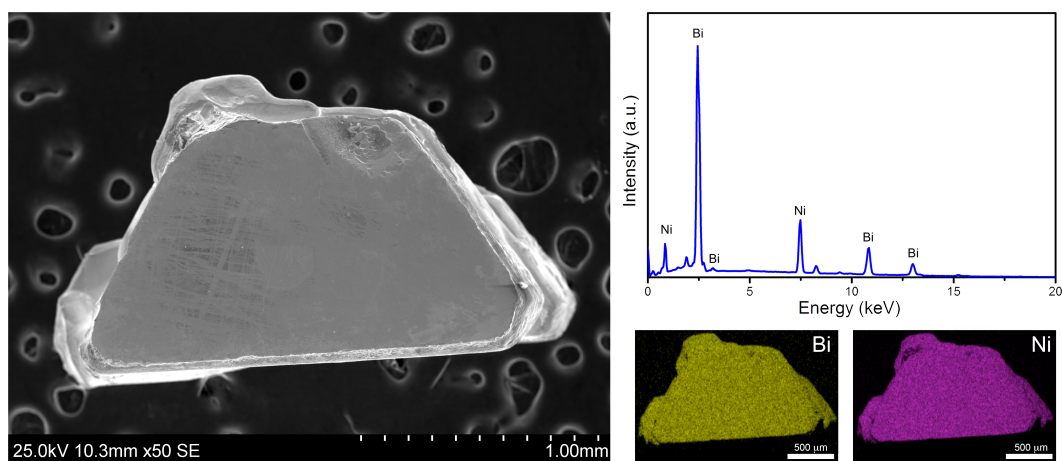


**Figure S2** | Secondary electron scanning electron microscopy (SEM) image of an  $\alpha$ -NiBi single crystal (left). Energy dispersive spectrum from point collection shows only Ni and Bi present in the spectrum (right top). Averaging the integrations of spectra collected at 15 points yields an atomic formula of  $\text{Ni}_{0.92}\text{Bi}$  (right top). Map spectra of Bi and Ni show homogeneous distribution of elements across the crystal, confirming the phase purity (right bottom).

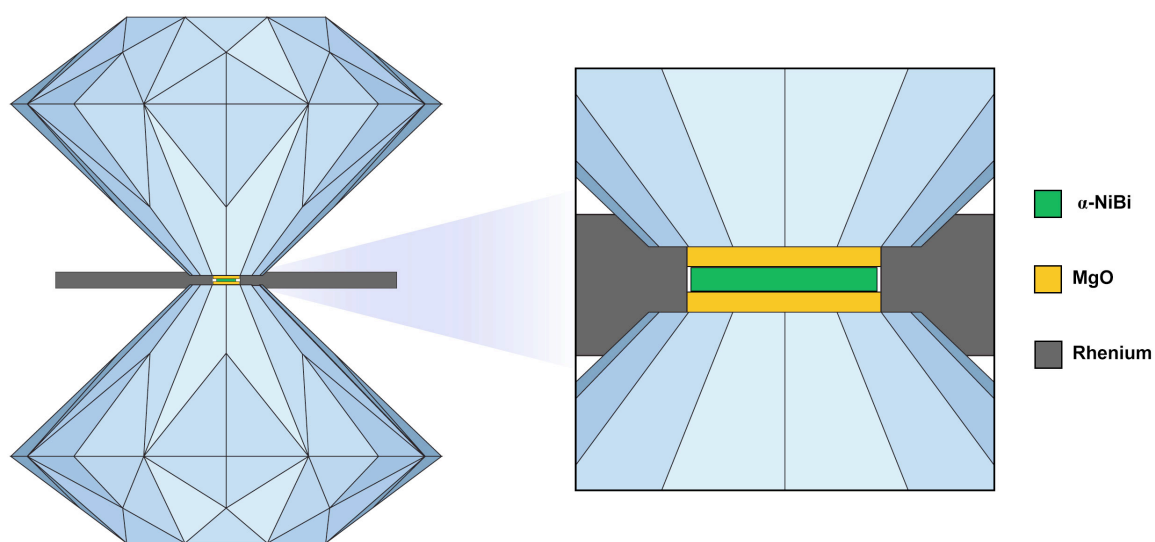


**Figure S3** | Side-view schematic of the DAC after closing the cell and before the initial pressurization. MgO discs are placed on the center of the upper and lower diamond culets. The sample, which is a powder of  $\alpha$ -NiBi crystals, is placed on top of the lower MgO piece. The top diamond is lowered carefully into place so that it settles into the indentation and delivers the upper MgO disc to the sample chamber.

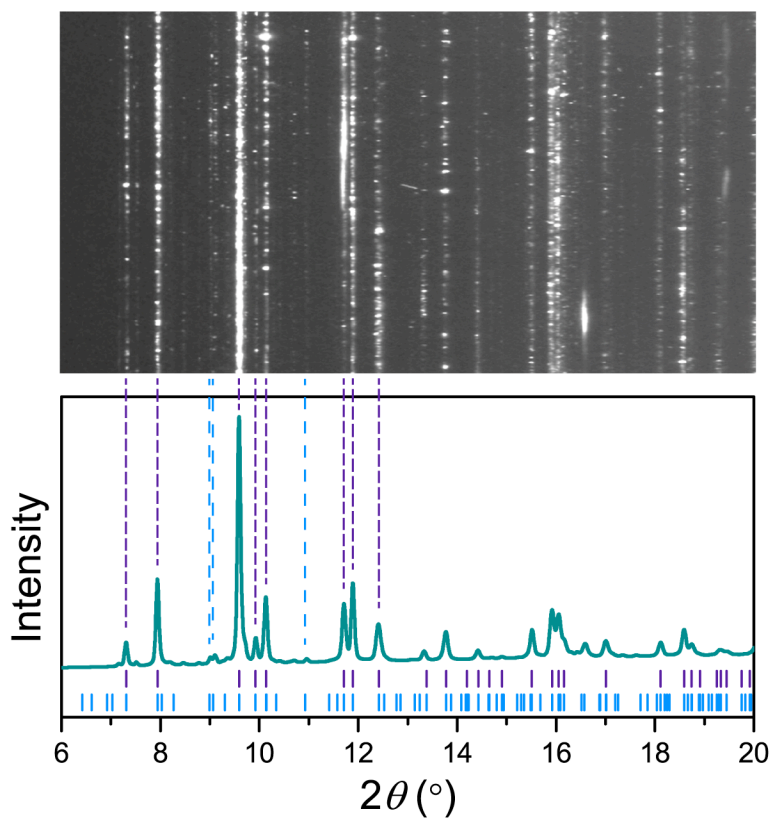


**Figure S4** | A slice of the 2D cake image (top) and corresponding integrated PXRD pattern (bottom) of the reaction site after cooling to ambient temperature ( $\lambda = 0.406626$  Å,  $P = 36.76(4)$  GPa). The dashed violet lines connect the most intense and continuous peaks from raw 2D image with their corresponding peaks in the integrated pattern. The dashed blue lines connect the weaker, potentially supercell reflections with their corresponding peaks. The violet and blue vertical markers below the experimental trace indicate the position of predicted Bragg reflections of the orthorhombic subcell and supercell, respectively, of the  $\beta$ -NiBi structure.

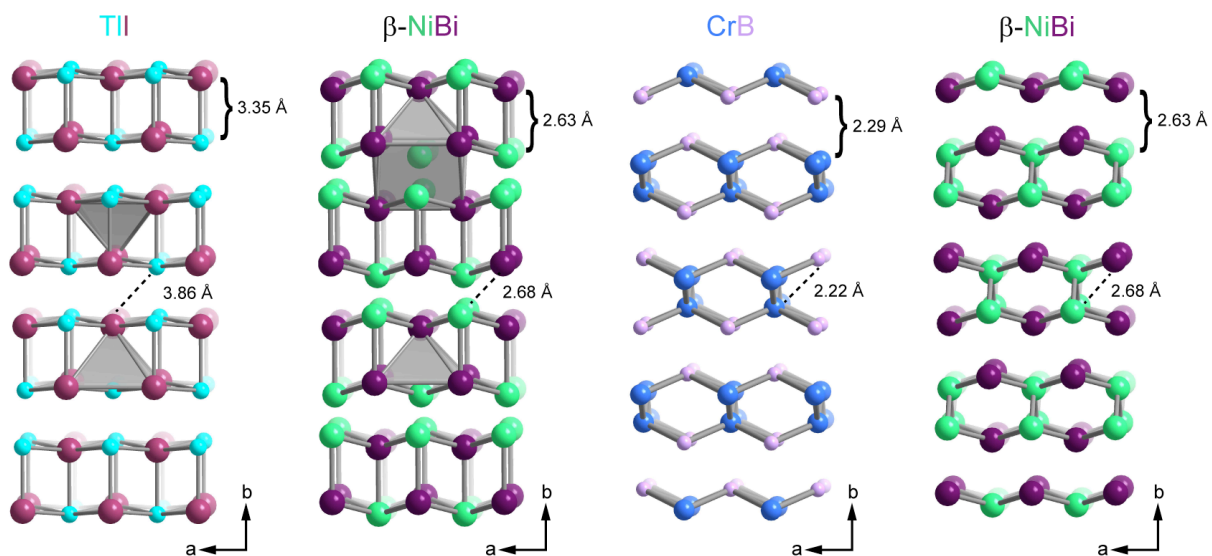


**Figure S5** | Crystal structure of  $\beta$ -NiBi compared to the TII structure type (left) and the anti-TII structure type, CrB (right). The text colors in the labels denote element identity in the structure. Interlayer and intralayer bond distances between the two atoms are shown to highlight that  $\beta$ -NiBi can be thought of as a compact version of the TII structure type. Two depictions of  $\beta$ -NiBi are presented, the one on the left showing the two shortest Ni–Bi bonds and the one on the right showing the shortest Ni–Bi bond and the Ni–Ni bonds.

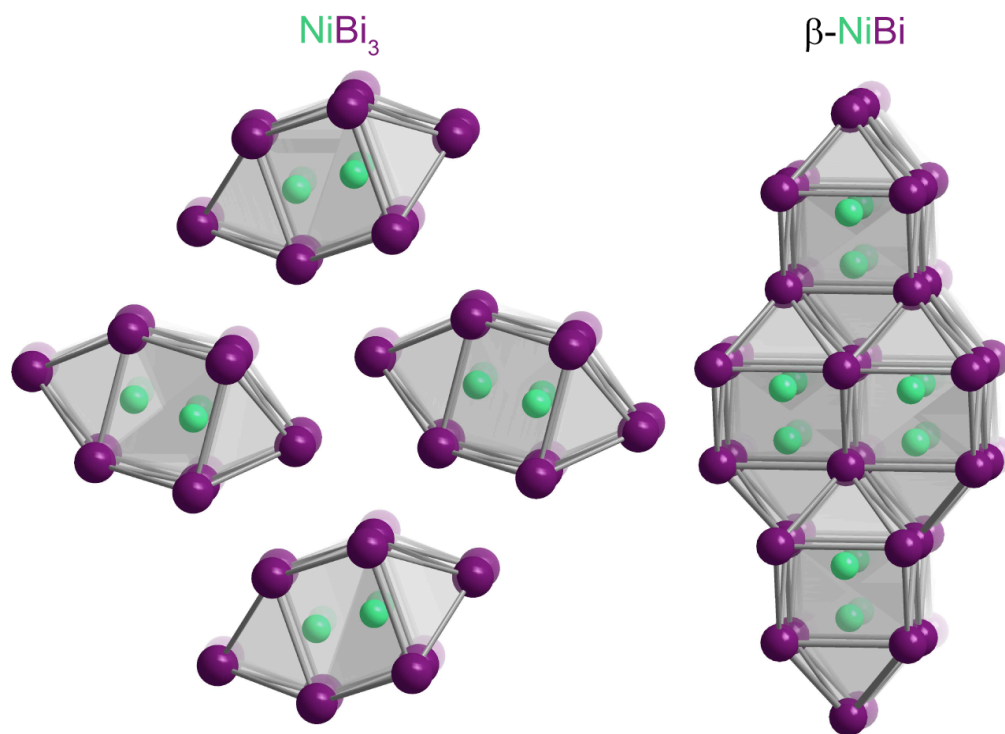


**Figure S6** | Structural comparison of the ambient pressure thermodynamically stable phase  $\text{NiBi}_3$  (left) and  $\beta\text{-NiBi}$  (right). The structure of  $\beta\text{-NiBi}$  can be thought of as a compact version of the  $\text{RhBi}_3$  structure type, where the rods are triangle-face sharing to form a 3-dimensional structure.

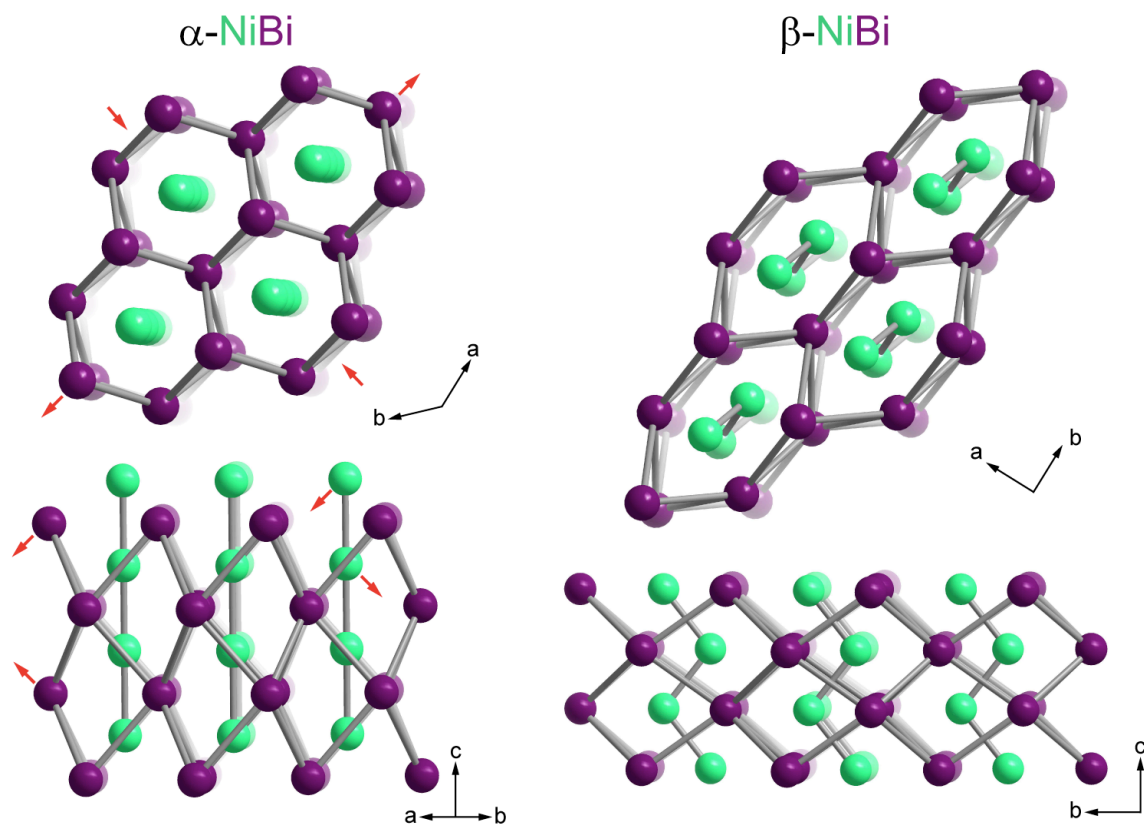


**Figure S7** | The subcell structure of  $\alpha$ -NiBi (left) compared to the structure of  $\beta$ -NiBi (right). Only Ni–Ni and Bi–Bi bonds are depicted to highlight that the general structural motif does not change significantly upon conversion from  $\alpha$ -NiBi to  $\beta$ -NiBi. The red arrows indicate the direction of the displacement of atoms from the  $\alpha$ -NiBi structure necessary to generate the  $\beta$ -NiBi structure. Most notably, there is a distortion in the hexagonal close packing of the Bi atoms and the linear chains of Ni atoms pucker to form zig-zag chains.

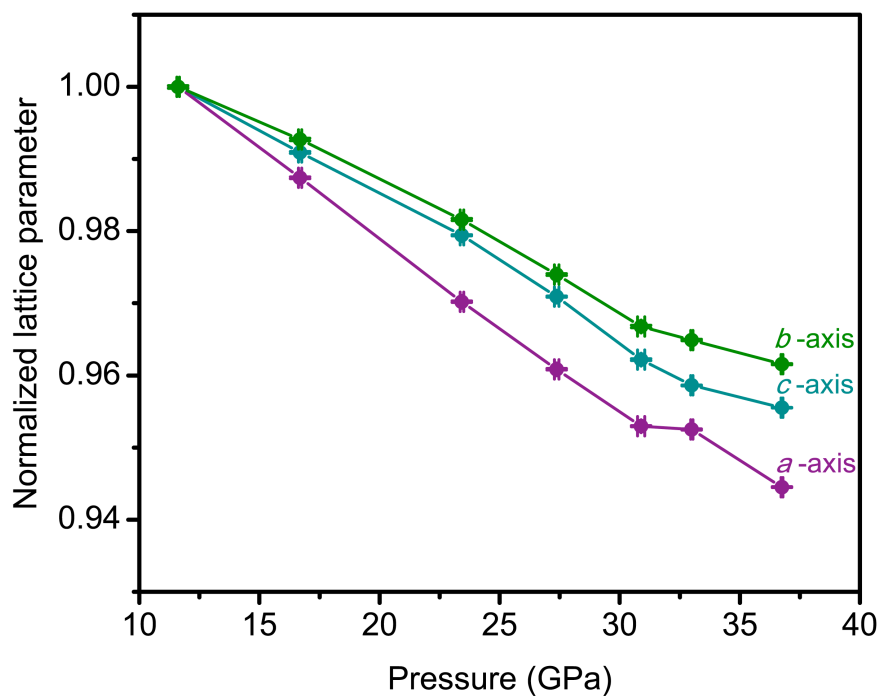


**Figure S8** | Experimental pressure dependence of the lattice parameters of  $\beta$ -NiBi upon decompression, normalized to the lowest pressure value at 11.62(6) GPa. Lines are drawn to guide the eye. The unit cell parameter *a* changes more rapidly with compression than *c*, which changes more rapidly with compression than *b*.

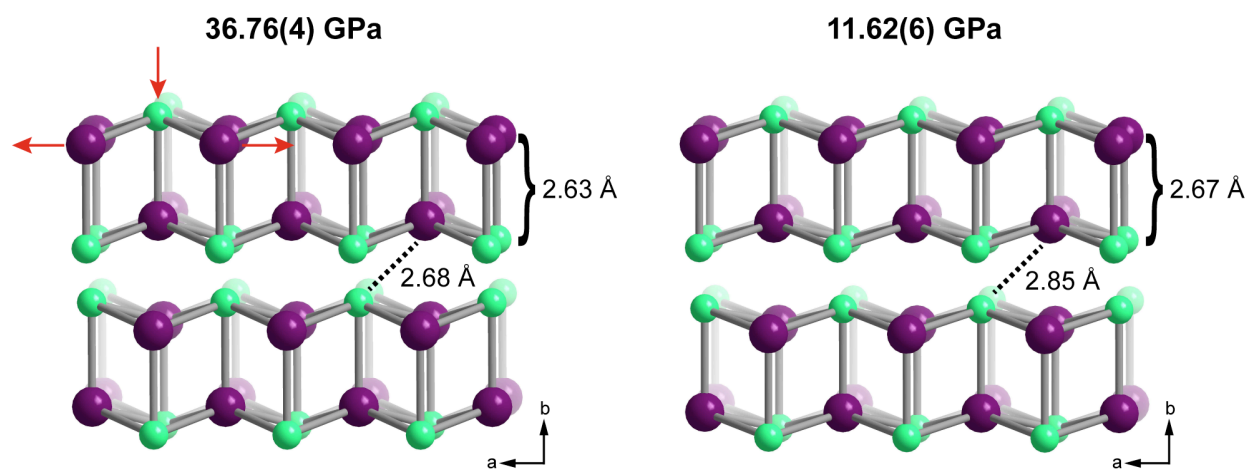


**Figure S9** | Comparison of the crystal structure of  $\beta$ -NiBi at 36.76(4) GPa (the synthesis pressure) and at 11.62(6) GPa (the lowest pressure at which it was observed). Notably, the percent difference between the interlayer and intralayer Ni-Bi interactions increases from 1.7% to 6.4%, indicating that the structure is becoming less compact and more layered as the pressure is released.

**Table S1** | Refinement details for  $\alpha$ -NiBi binary compound at 39.3(4) GPa.

<b>Phase 1: <math>\alpha</math>-NiBi</b>							
<b>Formula</b>	NiBi	<b>Double-Voigt Approach</b>			<b>Atomic parameters</b>		
<b><math>R_B</math></b>	2.450	<i>LVol-IB (nm)</i>	0	Site	<i>x</i>	<i>y</i>	<i>z</i>
<b>Space group</b>	<i>P6<sub>3</sub>/mmc</i>	<i>LVol-FWHM (nm)</i>	0	Bi1	0	0	0
<b><i>a</i> (Å)</b>	3.7763(5)	<i>e0</i>	0.0056(4)	Ni1	1/3	2/3	0.25
<b><i>c</i> (Å)</b>	4.9767(14)						
<b>Cell mass</b>	535.348						
<b>Cell volume (Å<sup>3</sup>)</b>	61.46(2)						
<b>Density (g cm<sup>-3</sup>)</b>	14.464(6)						
<b>Fraction (%)</b>	62(2)						
<b>Phase 2: MgO</b>							
<b>Formula</b>	MgO	<b>Double-Voigt Approach</b>			<b>Atomic parameters</b>		
<b><math>R_B</math></b>	2.171	<i>LVol-IB (nm)</i>	0	Site	<i>x</i>	<i>y</i>	<i>z</i>
<b>Space group</b>	<i>Fm<math>\bar{3}</math>m</i>	<i>LVol-FWHM (nm)</i>	0	Mg1	0	0	0
<b><i>a</i> (Å)</b>	3.9761(6)	<i>e0</i>	0.0015(10)	O1	0	0	0.5
<b>Cell mass</b>	161.218						
<b>Cell volume (Å<sup>3</sup>)</b>	62.86(3)						
<b>Density (g cm<sup>-3</sup>)</b>	4.259(2)						
<b>Fraction (%)</b>	38(2)						

**Table S2** | Refinement details for the new  $\beta$ -NiBi binary compound at 36.76(4) GPa.

Phase 1: $\beta$ -NiBi							
Formula	NiBi	Double-Voigt Approach		Atomic parameters			
$R_B$	1.419	<i>LVol-IB (nm)</i>	37.300	Site	<i>x</i>	<i>y</i>	<i>z</i>
Space group	<i>Cmcm</i>	<i>LVol-FWHM (nm)</i>	50.877	Bi1	0	0.1414(3)	0.25
<i>a</i> (Å)	3.3873(2)	<i>e0</i>	0.00127	Ni1	0	0.421(1)	0.25
<i>b</i> (Å)	9.4079(9)						
<i>c</i> (Å)	3.7587(2)						
Cell mass	1070.695						
Cell volume (Å <sup>3</sup> )	119.778(16)						
Density (g cm <sup>-3</sup> )	14.844(2)						
Fraction (%)	43.2(2)						

Phase 2: MgO							
Formula	MgO	Double-Voigt Approach		Atomic parameters			
$R_B$	0.349	<i>LVol-IB (nm)</i>	25.283	Site	<i>x</i>	<i>y</i>	<i>z</i>
Space group	<i>Fm<math>\bar{3}</math>m</i>	<i>LVol-FWHM (nm)</i>	25.483	Mg1	0	0	0
<i>a</i> (Å)	3.9875(2)	<i>e0</i>	0	O1	0	0	0.5
Cell mass	161.218						
Cell volume (Å <sup>3</sup> )	63.403(11)						
Density (g cm <sup>-3</sup> )	4.2223(7)						
Fraction (%)	56.8(12)						

**Table S3** | Comparison of different structural models for  $\beta$ -NiBi at 36.76(4) GPa. The  $b$ -axis of the orthorhombic cell is bolded to highlight the axis that tripled when moving to a superstructure. Upon converting symmetry, the orthorhombic  $b$ -axis switches to monoclinic  $a$ -axis.

Space group	$a$ (Å)	$b$ (Å)	$c$ (Å)	$\beta$ (°)	$wR$
<i>Cmcm</i>	3.3901(2)	<b>9.4020(6)</b>	3.7591(2)	90	4.208
<i>Cmcm</i>	3.3901(2)	<b>28.206(2)</b>	3.7591(2)	90	4.203
<i>C2/m</i>	<b>9.4014(6)</b>	3.3903(2)	3.7592(2)	89.95(2)	4.064
<i>C2/m</i>	<b>28.205(2)</b>	3.3902(2)	3.7592(2)	90.05(2)	4.042

**Table S4** | Pressure and unit cell parameters of  $\beta$ -NiBi during decompression.

<b>Pressure (GPa)</b>	<b><i>a</i> (Å)</b>	<b><i>b</i> (Å)</b>	<b><i>c</i> (Å)</b>
36.76(4)	3.3873(2)	9.4079(9)	3.7587(2)
33.00(4)	3.4160(3)	9.4407(10)	3.7708(3)
30.89(14)	3.4176(3)	9.4589(18)	3.7849(5)
27.37(10)	3.4459(4)	9.5295(12)	3.8192(3)
23.43(7)	3.4795(4)	9.6041(15)	3.8527(4)
16.69(7)	3.5411(5)	9.7128(18)	3.8979(5)
11.62(6)	3.5863(5)	9.7840(20)	3.9336(6)

## References

- 1 G. Voss, *Z. Anorg. Chem.*, 1908, **57**, 34-71.
- 2 P. C. Canfield and Z. Fisk, *Philos. Mag. B*, 1992, **65**, 1117-1123.
- 3 Bruker. APEX2, Version 2009.5-1: Data Collection and Processing Software; Bruker Analytical X-Ray Instruments, Inc.: Madison, WI, 2009.
- 4 V. D. Petricek, M. Dusek and L. Palatinus, *Z. Kristallogr.*, 2014, **229**, 345-352.
- 5 M. Ruck, *Z. Anorg. Allg. Chem.*, 1999, **625**, 2050-2054.
- 6 S. Lidin, V. Petricek, L. Stenberg, S. Furuseth, H. Fjellvag and A. Larsson, *Solid State Sci.*, 2000, **2**, 353-363.
- 7 J. P. S. Walsh, S. M. Clarke, Y. Meng, S. D. Jacobsen and D. E. Freedman, *ACS Cent. Sci.*, 2016, **2**, 867-871.
- 8 S. M. Clarke, M. Amsler, J. P. S. Walsh, T. Yu, Y. Wang, Y. Meng, S. D. Jacobsen, C. Wolverton and D. E. Freedman, *Chem. Mater.*, 2017, **29**, 5276-5285.
- 9 R. Hrubciak, S. Sinogeikin, E. Rod and G. Shen, *Rev. Sci. Instrum.* 2015, **86**, 072202.
- 10 Y. Meng, R. Hrubciak, E. Rod, R. Boehler and G. Shen, *Rev. Sci. Instrum.*, 2015, **86**, 72201.
- 11 C. Prescher and V. B. Prakapenka, *High Press. Res.*, 2015, **35**, 223-230.
- 12 A. A. Coelho, *TOPAS Academic: General Profile and Structure Analysis Software for Powder Diffraction Data*, Bruker AXS: Karlsruhe, Germany, 2007.
- 13 Inorganic Crystal Structure Database (ICSD) Web, Version 3.5.0, FIZ Karlsruhe, Germany, 2017.
- 14 P. Bhardwaj, S. Singh. Pressure induced structural phase transitions - a review. *Cent. Eur. J. Chem.* 2012, **10**, 1391-1422.
- 15 M. J. Buerger, *Phase Transitions in Solids*, Wiley, New York, 1951.
- 16 *International Tables for Crystallography*, ed. H. Wondratschek and U. Müller, Kluwer Academic Publishers, Dordrecht/Boston/London, **2004**, vol. A1, ch. 1, pp. 4-5
- 17 H. T. Stokes and D. M Hatch, *Isotropy Subgroups of the 230 Crystallographic Space Groups*, World Scientific, Singapore, 1988.
- 18 B. Markovic, D. Zivkovic, J. Vrest'al, D. Manasijevic, D. Minic, N. Talijan, J. Stajić-Trosić and R. Todorovic, *CALPHAD: Comput. Coupling Phase Diagrams Thermochem.*, 2010, **34**, 294-300.